Published in final edited form as:
Neuroimage. 2014 May 1; 91: 129–137. doi:10.1016/j.neuroimage.2013.12.061.

Motion compensation for brain PET imaging using wireless MR active markers in simultaneous PET-MR: phantom and non-human primate studies

Chuan Huang[1,2], **Jerome L. Ackerman**[2,3], **Yoann Petibon**[1,4], **Marc D. Normandin**[1,2], **Thomas J. Brady**[1,2], **Georges El Fakhri**[1,2], and **Jinsong Ouyang**[1,2,*]

Chuan Huang: huang.chuan@mgh.harvard.edu; Jerome L. Ackerman: jerry@nmr.mgh.harvard.edu; Yoann Petibon: petibon@pet.mgh.harvard.edu; Marc D. Normandin: normandin.marc@mgh.harvard.edu; Thomas J. Brady: tom@nmr.mgh.harvard.edu; Georges El Fakhri: elfakhri@pet.mgh.harvard.edu

[1]Center for Advanced Medical Imaging Sciences, Division of Nuclear Medicine and Molecular Imaging, Department of Imaging, Massachusetts General Hospital, Boston, MA 02114

[2]Department of Radiology, Harvard Medical School, Boston, MA 02115

[3]Athinoula A. Martinos Center for Biomedical Imaging, Department of Radiology, Massachusetts General Hospital, Charlestown, MA 02129

[4]Laboratoire d'imagerie fonctionnelle (LIF), UMRS-678 INSERM- Université Pierre et Marie Curie, CHU Pitié-Salpêtrière, Paris, France

Abstract

Brain PET scanning plays an important role in the diagnosis, prognostication and monitoring of many brain diseases. Motion artifacts from head motion are one of the major hurdles in brain PET. In this work, we propose to use wireless MR active markers to track head motion in real time during a simultaneous PET-MR brain scan and incorporate the motion measured by the markers in the listmode PET reconstruction.

Several wireless MR active markers and a dedicated fast MR tracking pulse sequence module were built. Data were acquired on an ACR Flangeless PET phantom with multiple spheres and a non-human primate with and without motion. Motions of the phantom and monkey's head were measured with the wireless markers using a dedicated MR tracking sequence module. The motion PET data were reconstructed using list-mode reconstruction with and without motion correction. Static reference was used as gold standard for quantitative analysis.

The motion artifacts, which were prominent on the images without motion correction, were eliminated by the wireless marker based motion correction in both the phantom and monkey experiments. Quantitative analysis was performed on the phantom motion data from 24 independent noise realizations. The reduction of bias of sphere-to-background PET contrast by active marker based motion correction ranges from 26% to 64% and 17% to 25% for hot (i.e., radioactive) and cold (i.e., non-radioactive) spheres, respectively. The motion correction improved

*Author to whom correspondence should be addressed: Jinsong Ouyang, Ph.D., Division of Nuclear Medicine and Molecular Imaging, Massachusetts General Hospital, 55 Fruit Street, White Building 427, Boston, MA 02114, Phone: +1-617-643-4843, ouyang.jinsong@mgh.harvard.edu.

the channelized Hotelling observer signal-to-noise ratio of the spheres by 1.2 to 6.9 depending on their locations and sizes.

The proposed wireless MR active marker based motion correction technique removes the motion artifacts in the reconstructed PET images and yields accurate quantitative values.

Keywords

active marker; brain PET; simultaneous PET-MR; motion correction

1. Introduction

Simultaneous Positron Emission Tomography (PET) and Magnetic Resonance (MR) imaging (PET-MR) is a novel and promising hybrid modality generating substantial interest in recent years. Individually, these two imaging modalities have complementary advantages and disadvantages in terms of sensitivity, molecular specificity, and spatial and temporal resolution. Their strengths may be integrated and provide new insights in neuroimaging through the concurrent acquisition of synergistic anatomical, functional and biochemical information (Mandeville et al., 2013; Sander et al., 2013).

Brain PET scanning plays an important role in the diagnosis, prognostication (Silverman et al., 2001), and monitoring of many brain diseases including dementia, which brings overwhelming burden to patients, families, and society (Mehta and Thomas, 2012). PET also plays an important role in neuroimaging of animals including non-human primates for radiotracer development (Gunn et al., 2011; Parker et al., 2012) and in understanding of brain diseases (Eberling et al., 2003; Howell and Murnane, 2011).

Motion artifacts from head motion are one of the major hurdles in brain PET. Dynamic brain PET studies can last more than one hour; voluntary and involuntary head motions are almost inevitable. This is particularly true in the elderly, or patients with dementia or movement disorders. Head restraints are often used to reduce head motion during the acquisition, but they cause discomfort for patients, and head movements still cannot be completely eliminated (Bloomfield et al., 2003). Furthermore, perturbation of neurochemical processes can be introduced by the stress caused by restraint in animal studies (Arnsten, 2000; Fueger et al., 2006). Anesthesia is also often used to keep animals still during acquisition; studies showed that anesthesia can also perturb the neurological process under study (Angel et al., 1999; Hendrich et al., 2001; Lindauer et al., 1993; Nakao et al., 2001; Patel et al., 2008; Tsukada et al., 2000; Tsukada et al., 1999).

Many approaches have been explored in the effort to correct motion artifacts. Depending on whether the motion is estimated from the acquired PET data or by other instrumentation, the approaches can be divided into two groups: auto-correction and assisted-correction. For the auto-correction techniques, the measured PET data are divided into temporal frames, and the motion is then estimated between temporal frames from the PET data. The estimated motion field can then be used to transform the reconstructed images (Friston et al., 1995; Tellmann et al., 2006; Woods et al., 1992) or the sinograms (Hutton et al., 2002; Kyme et al., 2003) of each temporal frame to a reference frame. The accuracy of motion estimation using this approach is limited by the noise of PET images, which increases as the data set is divided into temporal frames for a dynamic image sequence. Moreover, the fact that the motion estimation relies on the generation of images or sinograms limits its temporal resolution; this method is not suitable when the activity distribution is fast changing or the object is fast moving. The reconstruction algorithms of the assisted-correction approaches are similar to auto-correction techniques except that the motion information is instead measured using an

instrument other than the PET camera, such as video/infrared cameras (Bloomfield et al., 2003; Goldstein et al., 1997; Picard and Thompson, 1997), and approaches with structured light (Olesen et al., 2012; Olesen et al., 2013). Similar approaches have also been applied to motion correction in MRI (Schulz et al., 2012; Zaitsev et al., 2006). One advantage of these optical motion tracking approaches is that they are independent of the PET-MR acquisition, so that no changes to MR pulse sequence are required, in contrast to MR navigator-based methods. Another advantage is that the optical methods, in principle, are capable of achieving high frame rate. Some of these approaches monitor the motions of the reflectors attached to the subject's head; some observe a portion of the subject's face. But they all require an unobstructed view from the cameras to the reflectors or the subject's face. This is challenging for PET-MR head scan because the view from outside of the scanner is blocked by the head coil, especially for the modern head coils with large number of channels. There are RF contamination and MR compatibility issues associated with installing cameras inside of the scanner. Moreover, these optical systems require complicated calibrations.

Conventional MR navigator methods (Ehman and Felmlee, 1989; Wang et al., 1996) can be used to track motion with temporal resolution less than 20 ms. However, such methods cannot be used to track head rotation. Catana et al (Catana et al., 2011) used the cloverleaf navigator method (van der Kouwe et al., 2006) to track head motion for PET motion compensation. Although this method can track both translation and rotation, its motion tracking accuracy suffers from off-resonance effects, gradient instabilities, as well as signal contamination from non-rigid motion of the neck. Moreover, the cloverleaf navigator method requires approximately 20 seconds of motionless data to calibrate. Petibon et al (Petibon et al., 2013) used image-based MR motion tracking for non-rigid motion compensation in cardiac PET. However, it generally lacks temporal resolution because of the long scanning time needed for acquiring the entire image volume.

Motion monitoring using wired MR active markers dates back to 1986 (Ackerman et al., 1986). It has been used for prospective motion correction and device tracking in MR imaging (Derbyshire et al., 1998; Dumoulin et al., 1993). Recently, wireless MR active markers gained interest in the MR community for prospective motion correction due to its simpler manufacturing, easier setup and better patient-friendliness (Garnov et al., 2011; Ooi et al., 2013; Sengupta et al., 2013). In this work, we propose to use wireless MR active markers to track head motion in real time during a brain PET-MR scan and incorporate the motion measured by the markers in a modified listmode PET reconstruction algorithm. This makes PET images, which are reconstructed from data acquired on a simultaneous PET-MR scanner, free of motion artifacts. Phantom and non-human primate experiments were conducted to evaluate the proposed methods. Our method is dedicated to simultaneous PET-MR scanners.

2. Material and methods

2.1 Simultaneous PET-MR scanner

All acquisitions in this study were performed on a commercially available whole-body simultaneous PET-MR scanner (Siemens Biograph mMR, Siemens Healthcare, Erlangen, Germany). This scanner consists of an MR-compatible lutetium oxyorthosilicate (LSO) crystal based PET camera inside a 3 Tesla MR scanner, which provides 258 mm axial field of view and 4.4 mm full width at half maximum (FWHM) transverse spatial resolution at 1 cm off the center. The simultaneity and spatial alignment between PET and MR scanners are essential for performing MR-assisted motion correction in brain PET.

Accurate temporal alignment of the PET and MR data was ensured by using simulated electrocardiography (ECG) signals which are recorded in the PET listmode and

physiological signal logging on the MR scanner with a modification to the MR pulse sequence [code by Michael Erb, obtained from Siemens Integrated Development Environment for Applications (IDEA) discussion board www.mr-idea.com].

2.2 Motion tracking with wireless MR active markers

2.2.1 Active marker hardware—The wireless MR coils work by inductive coupling with the body RF coil of the scanner (and with the separate receiver coil if used). The RF magnetic field of the transmit pulse excites an RF current in the wireless coil, which in turn excites the spins in the water sample. Although the body coil-wireless coil mutual inductance is quite small, the RF field (B_1) produced in the water sample is quite large because of the large filling factor and the high quality factor (Q-factor) of the wireless coil, such that an RF flip angle of only a fraction of a degree (measured with respect to the body coil for the imaged subject, not the tracking sample) excites an intense signal from the wireless coil. Again, mutual inductance between the wireless coil and the receive coil (or body coil) couples the MR signal of the water sample into the receiver, yielding a readily detectable signal.

As shown in Figure 1, the wireless MR active markers were built by installing a solenoidal wireless MR miniature coil around a spherical microsample cell with a volume of 18 μL (model 529-A, Wilmad-LabGlass, Vineland, NJ, USA). The sphere was filled with a degassed solution of deionized water doped with 1.25g/L $NiSO_4$•$6H_2O$ and 5 g/L NaCl. The sphere was immersed in liquid nitrogen while the air was pumped out, and the neck was flame-sealed under vacuum. The MR coils were built by winding 4 turns of 14 AWG (American wire gauge; 1.63 mm diameter) bare copper wire into a solenoid about 9.1 mm long by 9.8 mm outside diameter, resulting in an inductance of about 82 nH. The capacitance required to resonate the coils at 123.14 MHz (the exact Larmor frequency of the Siemens “3T” scanner) is about 20 pF, which was made up with a combination of a fixed ATC (American Technical Ceramics, Huntington Station, NY, USA) nonmagnetic chip capacitor and an adjustable Johanson type 9341 nonmagnetic SMD (Surface Mount Device) trimmer capacitor (Johanson Manufacturing Corporation, Boonton, NJ, USA). Because the coils are not wired to an external circuit, no impedance matching circuitry is needed. The adjustable capacitor allowed the coil to be fine-tuned with the water sample in place by observing the resonance frequency while the coil is probed with a coupling loop connected to a Hewlett-Packard 8753C vector network analyzer displaying reflected power. The typical coil quality factor Q (a dimensionless measure of the sharpness of coil tuning) was on the order of 120 with the water sample inserted. The coils were enclosed in polypropylene tubes to prevent contact with the phantom or the skin of the subject. Additional coils were built similarly with finer gauge, e.g., 26 AWG (American Wire Gauge), insulated magnet wire using a larger number of turns in a close-wound solenoid. The coils using finer wire tended to exhibit higher Q but less stability in tuning, presumably because the finer wire was less rigid, this permitted inductance changes during handling. None of the coils in this study included back-to-back switching diodes to limit the RF excitation applied to the water sample, because the diodes tended to lower the Q as well as the detection sensitivity. In some cases propylene tubes (syringe barrels) were used to support the coil from the inside, provide a “handle” so that the coils could be handled or fixed to the object being imaged.

Safety testing of the wireless active markers was performed according to our institutional coil safety test procedure. The test was conducted with a standard series of pulse sequences designed to evoke maximum heating from RF or gradient eddy currents. All of the coils exhibited no more than barely detectable heating (2°C maximum).

2.2.2 Active marker tracking MR sequence—A dedicated MR sequence module as shown in Figure 2 was built to obtain the locations of the wireless active markers by measuring their X, Y, Z projections. The projections were measured by performing a gradient readout along the X, Y, Z directions (G_x, G_y, G_z) after a 60 μs non-selective RF excitation pulse with 1° flip angle. During the readout compensation gradient pulse, dephasing gradient pulses were applied in a direction perpendicular to the read-out gradients to attenuate the background signal from the object (Qin et al., 2013). Spoiler gradient pulses were applied after the gradient readout to eliminate spurious gradient echoes and avoid affecting other MR acquisitions performed afterwards. With a bandwidth of 1149 Hz/pixel, 256 readout points, 2 times readout oversampling, and 1.2 mm/pixel spatial resolution, the module takes less than 10 ms to obtain the positions of the wireless markers.

2.2.3 Motion field calculation—The projection locations of the markers are calculated by taking the centroid of the projection signal within an 11-pixel search window centered at the pixel with the highest signal intensity to enable a stable peak location measurement (Qin et al., 2013). In this work, the correspondence between the projections peaks and the markers are determined under the assumption that the projection displacement between two neighboring measurements is small. The correspondences between the individual markers and their initial X, Y and Z positions are initialized using prior knowledge about the placement of the markers.

The 3D locations of the markers are obtained by combining the corresponding X, Y and Z projection locations of the markers. Under the assumption that the head undergoes rigid motion, the transformation of the head is determined purely by a single 3D translation and rotation which can be uniquely determined by the translational displacements of three non-collinear wireless markers rigidly attached to the head. For any two measurements, a rotation matrix and a translation between these two measurements can be obtained using the algorithm developed by Arun, et al (Arun et al., 1987).

2.3 Motion correction in PET list-mode reconstruction

In theory, it is possible to perform motion correction for each time point independently. However, this approach will be quite time-consuming and computationally expensive. As a result, in this work, the time points are binned into the same motion phase when none of the three measured locations of wireless markers moved more than 2mm, an approach sometimes called multiple acquisition frames (Picard and Thompson, 1997). To put this into a mathematical expression, two time points are grouped into the same motion phase when:

$$\left|\overrightarrow{r_t^k} - \overrightarrow{r_{t'}^k}\right| < \beta \text{for} k = 1, 2, 3; \quad (1)$$

where $\overrightarrow{r_t^k}$ is a vector representing the 3D locations of the k^{th} wireless markers for time point t, and β = 2 mm, the distance threshold value used in this work, is intermediate between the tracking accuracy (on the order of 1 mm) and the PET scanner spatial resolution (on the order of 4 mm for the Biograph mMR).

Maximum-likelihood Expectation Maximization reconstruction algorithm, which includes its variations, has been the leading iterative reconstruction algorithm for PET. The algorithm approaches the true activity image by means of successive forward- and back-projections. An initial estimated image, such as an uniform image, is first assumed. The next step is to compute the sinograms that would have been measured for the estimated image using forward-projection, which is performed by summing up the intensities along the potential lines of response (LORs) for all the sinograms through the estimated image. The set of

sinograms generated from the estimated image is then compared to the actually measured sinograms. The ratio between the actually measured and estimated sinograms is back-projected to obtained updated images. Such forward-and back-projection process is repeated for a number of times. Given motion fields measured using wireless markers, a list-mode ordinary Poisson expectation maximization can be formulated as:

$$x_j^{k+1} = \frac{x_j^k}{\bar{s}_j} \sum_{n=1}^{N} \frac{a_{i_n,j}^m}{\sum_j^J, a_{i_n,j}^m, x_j^k, + \overline{Sc}_{i_n} + \overline{R}_{i_n}}, \quad (2)$$

where x_j^k is the activity in voxel *j* (*j* = 1,2, ⋯, *j*) at the k^{th} iteration, *N* is the number of detected PET events, $a_{i_n,j}^m$ is an element of the motion-dependent system matrix which is the probability for an event inside voxel j in motion phase *m* (*m* = 1,2, ⋯, *M*) to be detected along LOR i_n, where i_n (i_n = 1,2, ⋯, I) represents all the possible LORs of the scanner, $\bar{s}_j$ is the sensitivity for voxel j averaged over all motion phases. $\overline{Sc}_{i_n}$ and $\bar{R}_{i_n}$ are the estimates for average scatters and randoms along LOR i_n.

The measured motion field $\boldsymbol{M}_m$ of size $J \times J$, which transforms the image volume at the reference motion phase to motion phase *m*, is incorporated into the system matrix:

$$A^m = (a_{i_n,j}^m)_{I \times J} = \boldsymbol{S}\boldsymbol{T}_m \boldsymbol{P}\boldsymbol{M}_m, m = 1, 2, \cdots, M; \quad (3)$$

where P is the forward-projection matrix of size I × J which can be calculated based on Siddon's ray-tracing algorithm (Siddon, 1985) ; $\boldsymbol{S}$ and $\boldsymbol{T}_m$, both of size $I \times I$, are diagonal matrices providing respectively the LOR normalization factors and motion-dependent attenuation factors for motion phase *m*.

2.4 Phantom experiment

The proposed wireless MR active marker based motion correction technique for brain PET imaging was first evaluated in a phantom experiment.

2.4.1 Phantom experiment set-up—In the phantom experiment, we placed four hollow spheres (outer diameters = 33.3, 26.8, 21.8, 11.9 mm, wall thickness is 1 to 1.5 mm) and two solid spheres (diameters = 25.4, 19.1mm) inside ACR (American College of Radiology) Flangeless phantom (Data Spectrum Corporation, Hillsborough, NC, USA) with was used. The hollow spheres were filled with ^{18}F with activity concentration approximately 4 times the background activity concentration. The activity within the entire phantom was about 1.6 mCi at the beginning of the data acquisition.

Three wireless MR active markers were fixed to the surface of the phantom using adhesive tape. Because the signal of the active marker disappears if the axis of the marker is aligned with the static main (B_0) field of the MR scanner (Garnov et al., 2011), the markers were mounted such that their axes were roughly perpendicular to B_0 field.

As shown in Figure 3, the phantom was put onto a slope; and a ventilator driven balloon was placed next to the phantom to introduce complex motion involving both translation and rotation. The phantom rolls up the slope when the balloon is inflated, and rolls back as the balloon is deflated, resulting in up to approximately 3 cm translation and 15 degree rotation. In this experiment, the rate of the motion was set to 65 cycles/min.

Static list-mode data were first acquired for 20 min while the ventilator was off. After that, the ventilator was turned on and 56 min of dynamic PET listmode data were acquired. The motion of the phantom was tracked every 42 ms using the wireless markers and the

dedicated MR pulse sequence module. As stated above, each location measurement takes approximately 10 ms. PET imaging does not require this high frame rate. Instead of acquiring the tracking module continuously, the tracking sequence module was performed every 42 ms in the phantom study to mimic the typical timing as if the tracking module was inserted into other MR sequences. Inserting the tracking module into other MR sequences enables active marker based motion tracking while performing other MR sequences.

Attenuation maps of the wood slope and the ACR phantom were generated by a separate CT scan acquired afterwards. The attenuation map of the scanner hardware, which was acquired and stored by Siemens, was also obtained from the console as an image volume which was generated by the scanner automatically. Because wood is not detectable in the MR scan, several vitamin E capsules were embedded in the wood slope as markers to visualize it and allow proper positioning of the wood slope for the generation of the combined attenuation map. The attenuation map of the phantom was also transformed by the measured motion field to provide proper attenuation at different motion phases.

2.4.2 Quantitative assessment of the phantom data—To perform statistical image quality assessment of the method, the 56-min dynamic PET listmode data were divided temporally into 24 independent noise realizations with the same duration. The number of motion phases used in the image reconstruction was about 100. Each realization was reconstructed with:

1. MC: reconstructed with wireless MR active marker based motion correction described in Section 2.3.
2. nMC: reconstructed without motion correction using the attenuation map at the reference phase (corresponding to the static position).

In addition, a gold standard image was also reconstructed from the 20-min static list-mode data.

All reconstructions were performed on 4.17×4.17×2.03 mm voxel grid with 10 iterations and 8 temporal subsets. The reconstructed images were resampled onto a 4.17×4.17×4.06 mm grid after being smoothed by a 3D Gaussian smoothing filter with FWHM = 4 mm.

Objective image quality assessment was performed using:

a. **Contrast analysis**: six spherical Volumes Of Interest (VOI) corresponding to the 6 spheres (4 hollow and 2 solid) were drawn on the CT image. The mean (c_i^k) contrast values of these 6 VOIs (i = 1, ⋯, 6) for noise realization k (k = 1 ⋯, 24) are calculated as:

$$c_i^k = \frac{a_i^k - b_i^{\boldsymbol{k}}}{b_i^{\boldsymbol{k}}}, \quad (4)$$

where a_i^k is the average activity concentration in the i^{th} VOI; $b_i^{\boldsymbol{k}}$ is the average activity concentration of the background voxels surrounding the i^{th} VOI. The mean and standard deviation of the average contrast value errors were then calculated for MC and nMC respectively where the corresponding contrast values obtained from the static reference image were used as the gold standards.

b. **Lesion detectability analysis**: A Channelized Hotelling Observer (CHO) was applied to the same 6 VOIs for the lesion detectability study. CHO has been shown to be good predictor of human observer performance in lesion detectability (Gifford et al., 2000), and the spheres were treated as lesions in this analysis. The matrix

size used was 13×13×13 voxels. A five-channel 3D Laguerre-Gauss filter was used for the CHO. Due to the lack of "lesion-absent" data, the size-matched lesion-absent VOIs were drawn in the center of the phantom where the activity concentration is uniform, and the same slices as the "lesion-present" VOIs were selected.

2.5 *In vivo* experiment

The *in vivo* experiment was authorized by the Institutional Care and Use Committee at Massachusetts General Hospital and performed in compliance with our approved protocol. A rhesus macaque monkey was anesthetized with isoflurane (1% inhaled in 100% oxygen) during the study. 4.85 mCi of ^{18}F-FDG was administered by intravenous injection 120 min prior to the PET-MR acquisition. During the uptake period, three wireless MR active markers were attached to a cranial post rigidly fixed to the skull for head immobilization in other studies (Vanduffel et al., 2001). The monkey was positioned in the bore of the scanner with the wireless active markers having several cm clearance from the MR head coil with the left side of animal's head resting on a small pillow. The pillow was attached to a cord accessible from outside the scanner. The inside of the MR head coil was also padded with towels to avoid traumatic head motion. When the pillow was pulled out, the monkey's head rolled to its left and onto the padding towels.

Two 5-min PET list-mode acquisitions were performed sequentially. No motion was introduced in the first 5-min acquisition. During the second 5-min acquisition, the pillow was manually removed by the cord 3 min into the scan to induce motion. The MR active marker tracking sequence module was performed every 50 ms throughout the entire scan for both acquisitions.

Similarly to the image reconstruction from the phantom data, MC and nMC reconstructions were performed on the second 5-min acquisition, and the data from first 5-min acquisition were reconstructed with nMC as static reference. The MC reconstruction was performed using 2 motion phases based on the nature of the motion. The images were reconstructed on a 2×2×2 mm grid after being smoothed by a 3D Gaussian smoothing filter with FWHM = 4 mm.

3. Results

One set of the X, Y, Z projections acquired at the same time point during the phantom experiment is shown in Figure 4. As shown here, the X, Y, Z projections of the 3 wireless MR active markers can be easily identified from the background noise.

Figure 5 shows the traces of the 3 wireless markers in the X, Y, Z projections during a 4 s period. The figure shows the motion of the wireless markers in the projections. Again, the traces of the wireless markers can be easily identified from the background. The 3D locations of the 3 markers can be obtained using the traces for any time point during the 4 s period shown here. The rigid motion fields which were later incorporated into the system matrix of the PET listmode reconstruction as detailed in Section 2.3 can then be derived from the marker locations.

To demonstrate the effect of the dephaser gradients shown in Figure 2, the X projections of one wireless marker attached to a water phantom acquired with and without dephaser are shown in Figure 6. During the acquisition, the body RF coil was used for reception. The dephaser removed the signal of the phantom while preserving the signal of the active marker.

Figure 7 shows the images reconstructed from data of one noise realization with and without wireless marker based motion correction. A static image with approximately 10 times more events is also shown as the reference. Motion artifacts are prominent in the image reconstructed without motion correction. The spheres are blurred, and sphere 1 (hot, i.e., radioactive) and sphere 5 (cold, i.e., non-radioactive) are hardly visible in the image. When wireless marker based motion correction was applied to the same data set, the motion artifacts were completely removed. The contrasts of sphere 1 and 5 are nicely recovered and the motion corrected image agrees well with the static reference.

Besides visual comparison, quantitative image analysis was also performed using the phantom data as detailed in Section 2.4.2. Figure 8 shows the biases of the contrast values of the 6 spheres (numbering is shown in the right panel of Figure 7) obtained from the MC and nMC image volumes. As shown in this figure, the contrast value biases obtained from MC images are below 11% and 4% for the 4 hot spheres and 2 cold spheres respectively. However, the contrast values estimated from the nMC image volumes are systematically lower for the hot spheres and higher for the cold spheres. The biases of the contrast values obtained from images reconstructed using nMC can be as large as 75.0% and 27.9% for the hot and cold spheres respectively.

CHO analysis results are shown in Figure 9. When wireless MR marker based motion correction was used, the CHO signal-to-noise ratio (SNR) improvement was significantly (in the range of 1.2 to 6.9) for all spheres compared to the SNR obtained from images reconstructed without motion correction. The mean CHO SNR was improved by 235% for sphere 1 which is the smallest hot sphere and which suffers the largest motion blurring.

The reconstructed images of the *in vivo* study are shown in Figure 10a. Severe motion blurring can be seen in the nMC images. The movement consists of approximately 2 cm of translation and 10° of rotation, which is consistent with other previous studies (Montgomery et al., 2006; Olesen et al., 2012). When motion correction was performed, the blurring was eliminated from the reconstructed images, achieving similar image quality to the static reference. The profiles of the line shown in the top left panel are presented in Figure 10b. The MC profile matches well with the profile obtained from the static reference while the profile obtained from the nMC image is dramatically different. This further confirms the fact that the quality of the images reconstructed using wireless MR active marker based motion correction from data corrupted by head motion is similar to the quality obtained from motionless data acquired in the same duration.

4. Discussion

It can be seen from Figure 4 that the projection of each wireless MR active marker spans several pixels in every projection. The centroid approach used in this work for marker location calculation solves the ambiguity problem for the active markers with two peaks in their profiles (for example, Y projection of wireless marker 2 in Figure 4). The diameter of the water specimen placed in each active marker is approximately 3 mm. The projection resolution was 1.2 mm/pixel. It is possible to conservatively estimate the centroid of its projection with approximately 1 mm accuracy. With the same centroid algorithm for marker location determination, similar marker sample size, and similar MR parameters, Qin et al (Qin et al., 2013) reported 0.7 ± 0.5 mm (mean ± standard deviation), 0.6 ± 0.4 mm and 0.1 ± 0.1 mm spatial accuracy for the X, Y and Z directions projections respectively.

Although it is intuitive to assume perfect spatial alignment between PET and MR, the spatial accuracy of MR is affected by gradient non-linearity induced spatial distortion especially at the locations far from the scanner isocenter. When not corrected, the spatial distortion can

lead to misalignment between the attenuation map and emission image, and error in motion tracking. The gradient non-linearity was measured when the scanner was installed and the parameters are stored on the scanner, allowing to account for it. The spatial distortion correction can be performed off-line (Jovicich et al., 2006). The spatial distortion correction was not performed in our studies because the markers were close to the isocenter of the scanner, where the distortion caused by gradient nonlinearity was small. Also, due to the small displacements of the markers, gradient non-linearity had only second-order effects on the accuracy of our measurements.

The MR tracking sequence module shown in Figure 2 can be incorporated into other clinical MR imaging sequences. Because of the small flip angle needed (1° in this work), minimal impact to the host MR sequence is ensured. As a result, this tracking module can be incorporated into most gradient-echo (including ultra-short TE), spin-echo and echo-planar imaging sequences with the exception of certain steady-state free precession sequences. Also, by incorporating the module into other MR sequences, it allows motion corrected MR acquisition. The same motion measurements can be used to perform prospective motion correction during MR acquisition (Ooi et al., 2013). This can fully exploit the potential of simultaneous PET-MR scans in brain imaging. Besides brain PET and MR imaging, the proposed technique could also aid acquisitions in areas where subject bulk motion affects the results such as dynamic cardiac perfusion studies.

In Figure 5, the traces of the wireless markers do not overlap. In practice, the traces may cross each other if the markers are not placed far apart from each other. When that happens, the correspondence between the markers and the traces can still be determined by utilizing the constraint that the distances between the active markers remain the same under rigid motion. One measurement generates three locations on each of the X, Y and Z projections. In total, there are $3^3 = 27$ possible 3D locations for the three markers. Out of which there are 36 possible combinations forming a triangle as they should be. The triangle with the edge lengths that match with the initial placement will be selected. This was discussed in detail by Ooi et al (Ooi et al., 2013) and Sengupta et al. (Sengupta et al., 2013). Moreover, if the locations were frequently measured (as what was done in this work), the constraint that the displacement of each marker is small between two measurements can also be used for the correspondence determination.

The motion experienced by the phantom is a rolling motion. As a result, the higher the sphere is in the phantom (Figure 7), the stronger the motion it experiences. This is one of the reasons why sphere 4 shows the least improvement in CHO SNR when motion correction was performed. Another reason is that the size of sphere 4 is the largest; hence the motion blurring is least pronounced among the spheres.

Because of the small internal volume of sphere 1, all its voxels suffered from partial volume effect. In fact, when the motion is not corrected, the mean contrast value of the sphere 1 is only 1.14, which is hardly visible in the image. This is also confirmed by the CHO analysis, in which its CHO-SNR is only 0.26. However, when the motion is corrected, the contrast is much better recovered such that its mean contrast value increased to 0.50 which is close to 0.56 obtained from the static reference. The CHO-SNR was also improved to 4.22 from 1.26 by motion correction.

Although the contrast analysis shown in Figure 8 used the mean contrast values of the VOIs, an analysis using the maximal contrast value for the hot spheres and minimal contrast value for the cold spheres were also performed. The result was the same.

Comparing to wired active markers (Qin et al., 2013), wireless markers eliminated the cable connected to the miniature coils which is a source of potential RF heating and a source of

locally increased power deposition. Furthermore, the elimination of the long cables simplifies the subject preparation and also improves the reliability of the instrumentation due to less hardware needed. These advantages make wireless active marker more favorable in clinical setting compared to the wired approach. After ongoing approval from our institutional review board is completed, the technique demonstrated in this work will be further evaluated on patients undergoing brain PET/MR scans. To ensure the wireless markers rigidly follow the motion of the head, head band or plastic eye-glass frame will be used similar to what was done previously (Ooi et al., 2013; Ooi et al., 2009).

5. Conclusions

In this work, a wireless MR active marker based motion correction technique for PET brain imaging was proposed and validated using phantom and *in vivo* data acquired with a simultaneous PET-MR scanner. It has been shown that the motion artifacts can be removed with the proposed technique.

Acknowledgments

This research was supported in part by National Institutes of Health (NIH) grants R21-EB012326, R01-CA165221, R01-MH100350, the Athinoula A. Martinos Center for Biomedical Imaging, and the Center for Functional Neuroimaging Technologies (funded by NIH grant P41-EB015896).

References

Ackerman J, Offutt M, Buxton R, Brady T. Rapid 3D tracking of small RF coils. Proc Soc Magn Reson Med. 1986; 5:1131–1132.

Arnsten A. Stress impairs prefrontal cortical function in rats and monkeys: role of dopamine D1 and norepinephrine alpha-1 receptor mechanism. Prog Brain Res. 2000; 126:183–192. [PubMed: 11105647]

Arun KS, Huang TS, Blostein SD. Least-squares fitting of two 3-D point sets. IEEE Transactions on Pattern Analysis and Machine Intelligence PAMI-9. 1987:698–700.

Bloomfield P, Spinks T, Reed J, Schnorr L, Westrip A, Livieratos L, Fulton R, Jones T. The design and implementation of a motion correction scheme for neurological PET. Phys Med Biol. 2003; 48:959–978. [PubMed: 12741495]

Catana C, Benner T, van der Kouwe A, Byars L, Hamm M, Chonde DB, Michel CJ, El Fakhri G, Schmand M, Sorensen AG. MRI-assisted PET motion correction for neurologic studies in an integrated MR-PET scanner. J Nucl Med. 2011; 52:154–161. [PubMed: 21189415]

Derbyshire JA, Wright GA, Henkelman RM, Hinks RS. Dynamic scan-plane tracking using MR position monitoring. J Magn Reson Imaging. 1998; 8:924–932. [PubMed: 9702895]

Dumoulin C, Souza S, Darrow R. Real-time position monitoring of invasive devices using magnetic resonance. Magn Reson Med. 1993; 29:411–415. [PubMed: 8450752]

Eberling J, Cunningham J, Pivirotto P, Bringas J, Daadi M, Bankiewicz K. In vivo PET imaging of gene expression in parkinsonian monkeys. Molecular Therapy. 2003; 8:873–875. [PubMed: 14664788]

Ehman R, Felmlee J. Adaptive technique for high-definition MR imaging of moving structure. Radiology. 1989; 173:255–263. [PubMed: 2781017]

Friston K, Ashburner J, Frith C, et al. Spatial registration and normalization of images. Human Brain Map. 1995; 2:165–189.

Fueger B, Czernin J, Hildebrandt I, Tran C, Halpern B, Stout D, Phelps M, Weber W. Impact of animal handling on the results of ^{18}F-FDG PET studies in mice. J Nucl Med. 2006; 47:999–1006. [PubMed: 16741310]

Garnov N, Thormer G, Trampel R, Grunder W, Kahn T, Moche M, Busse H. Suitability of miniature inductively coupled RF coils as MR-visible markers for clinical purposes. Med phys. 2011; 38:6327. [PubMed: 22047397]

Gifford HC, King MA, De Vries DJ, Soares EJ. Channelized hotelling and human observer correlation for lesion detection in hepatic SPECT imaging. J Nucl Med. 2000; 41:514. [PubMed: 10716327]

Goldstein S, Daube-Witherspoon M, Green M, et al. A head motion measurement system suitable for emission computed tomography. IEEE Trans Med Imaging. 1997; 16:17–27. [PubMed: 9050405]

Gunn RN, Murthy V, Catafau AM, Searle G, Bullich S, Slifstein M, Ouellet D, Zamuner S, Herance R, Salinas C. Translational characterization of [11C] GSK931145, a PET ligand for the glycine transporter type 1. Synapse. 2011; 65:1319–1332. [PubMed: 21688322]

Howell LL, Murnane KS. Nonhuman primate positron emission tomography neuroimaging in drug abuse research. Journal of Pharmacology and Experimental Therapeutics. 2011; 337:324–334. [PubMed: 21317354]

Hutton B, Kyme A, Lau Y, et al. A hybrid 3-D reconstruction/registration algorithm for correction of head motion in emission tomography. IEEE Trans Nucl Sci. 2002; 49:188–194.

Jovicich J, Czanner S, Greve D, Haley E, van der Kouwe A, Gollub R, Kennedy D, Schmitt F, Brown G, MacFall J. Reliability in multi-site structural MRI studies: effects of gradient non-linearity correction on phantom and human data. Neuroimage. 2006; 30:436–443. [PubMed: 16300968]

Kyme A, Hutton B, Hatton R, et al. Practical aspects of a data-driven motion correction approach for brain SPECT. IEEE Trans Med Imaging. 2003; 22:722–729. [PubMed: 12872947]

Mandeville JB, Sander CY, Jenkins BG, Hooker JM, Catana C, Vanduffel W, Alpert NM, Rosen BR, Normandin MD. A receptor-based model for dopamine-induced fMRI signal. Neuroimage. 2013; 75:46–57. [PubMed: 23466936]

Mehta L, Thomas S. The role of PET in dementia diagnosis and treatment. Appl Radiol. 2012; 41:8–15.

Montgomery AJ, Thielemans K, Mehta MA, Turkheimer F, Mustafovic S, Grasby PM. Correction of head movement on PET studies: comparison of methods. J Nucl Med. 2006; 47:1936–1944. [PubMed: 17138736]

Olesen O, Sullivan J, Mulnix T, Paulsen R, Hojgaard L, Roed B, Carson R, Morris E, Larsen R. List-Mode PET Motion Correction Using Markerless Head Tracking: Proof-of-Concept With Scans of Human Subject. IEEE Trans Med Imaging. 2012; 32:200–209. [PubMed: 23008249]

Olesen, OV.; Paulsen, RR.; Jensen, RR.; Keller, SH.; Sibomana, M.; Højgaard, L.; Roed, B.; Larsen, R. Image-Based Geometric Modeling and Mesh Generation. Springer; 2013. 3D Surface Realignment Tracking for Medical Imaging: A Phantom Study with PET Motion Correction; p. 11-19.

Ooi MB, Aksoy M, Maclaren J, Watkins RD, Bammer R. Prospective motion correction using inductively coupled wireless RF coils. Magn Reson Med. 2013; 70:639–647.

Ooi MB, Krueger S, Thomas WJ, Swaminathan SV, Brown TR. Prospective real-time correction for arbitrary head motion using active markers. Magn Reson Med. 2009; 62:943–954. [PubMed: 19488989]

Parker CA, Gunn RN, Rabiner EA, Slifstein M, Comley R, Salinas C, Johnson CN, Jakobsen S, Houle S, Laruelle M. Radiosynthesis and Characterization of 11C-GSK215083 as a PET Radioligand for the 5-HT6 Receptor. J Nucl Med. 2012; 53:295–303. [PubMed: 22223878]

Picard Y, Thompson C. Motion correction of PET images using multiple acquisition frames. IEEE Trans Med Imaging. 1997; 16:137–144. [PubMed: 9101323]

Qin L, Schmidt EJ, Tse ZT, Santos J, Hoge WS, Tempany-Afdhal C, Butts-Pauly K, Dumoulin CL. Prospective motion correction using tracking coils. Magn Reson Med. 2013; 69:749–759. [PubMed: 22565377]

Sander CY, Hooker JM, Catana C, Normandin MD, Alpert NM, Knudsen GM, Vanduffel W, Rosen BR, Mandeville JB. Neurovascular coupling to D2/D3 dopamine receptor occupancy using simultaneous PET/functional MRI. Proc Natl Acad Sci USA. 2013

Schulz J, Siegert T, Reimer E, Labadie C, Maclaren J, Herbst M, Zaitsev M, Turner R. An embedded optical tracking system for motion-corrected magnetic resonance imaging at 7T. Magnetic Resonance Materials in Physics, Biology and Medicine. 2012; 25:443–453.

Sengupta S, Tadanki S, Gore JC, Welch EB. Prospective real-time head motion correction using inductively coupled wireless NMR probes. Magn Reson Med. 2013 10.1002/mrm.25001.

Siddon RL. Fast calculation of the exact radiological path for a three-dimensional CT array. Med phys. 1985; 12:252–255. [PubMed: 4000088]

Silverman DH, Small GW, Chang CY, Lu CS, de Aburto MAK, Chen W, Czernin J, Rapoport SI, Pietrini P, Alexander GE. Positron emission tomography in evaluation of dementia. J Am Med Assoc. 2001; 286:2120–2127.

Tellmann L, Fulton R, Pietrzyk U, al e. Concepts of registration and correction of head motion in positron emission tomography. Z Med Phys. 2006; 16:67–74. [PubMed: 16696372]

van der Kouwe AJ, Benner T, Dale AM. Real-time rigid body motion correction and shimming using cloverleaf navigators. Magn Reson Med. 2006; 56:1019–1032. [PubMed: 17029223]

Vanduffel W, Fize D, Mandeville JB, Nelissen K, Van Hecke P, Rosen BR, Tootell RB, Orban GA. Visual motion processing investigated using contrast agent-enhanced fMRI in awake behaving monkeys. Neuron. 2001; 32:565–577. [PubMed: 11719199]

Wang Y, Grimm R, Felmlee J, Riederer S, Ehman R. Algorithms for extracting motion information from navigator echoes. Magn Reson Med. 1996; 36:117–123. [PubMed: 8795030]

Woods R, Cherry S, Mazziotta J. Rapid automated algorithm for aligning and reslicing PET images. J Comput Assist Tomogr. 1992; 16:620–633. [PubMed: 1629424]

Zaitsev M, Dold C, Sakas G, Hennig J, Speck O. Magnetic resonance imaging of freely moving objects: prospective real-time motion correction using an external optical motion tracking system. Neuroimage. 2006; 31:1038–1050. [PubMed: 16600642]

Highlights

- Motion correction in brain PET using wireless MR active markers was validated
- The measured motion fields were incorporated into the PET listmode reconstruction
- The temporal resolution of the motion tracking can be better than 10ms
- Contrast recovered by motion correction is close to the static reference

Figure 1. Wireless active marker

a) A flame-sealed 18 μL spherical NMR microsample bulb filled with doped water, a US one-cent coin (19.05 mm in diameter), and solenoidal wireless MR coil; b) the assembled wireless MR active marker.

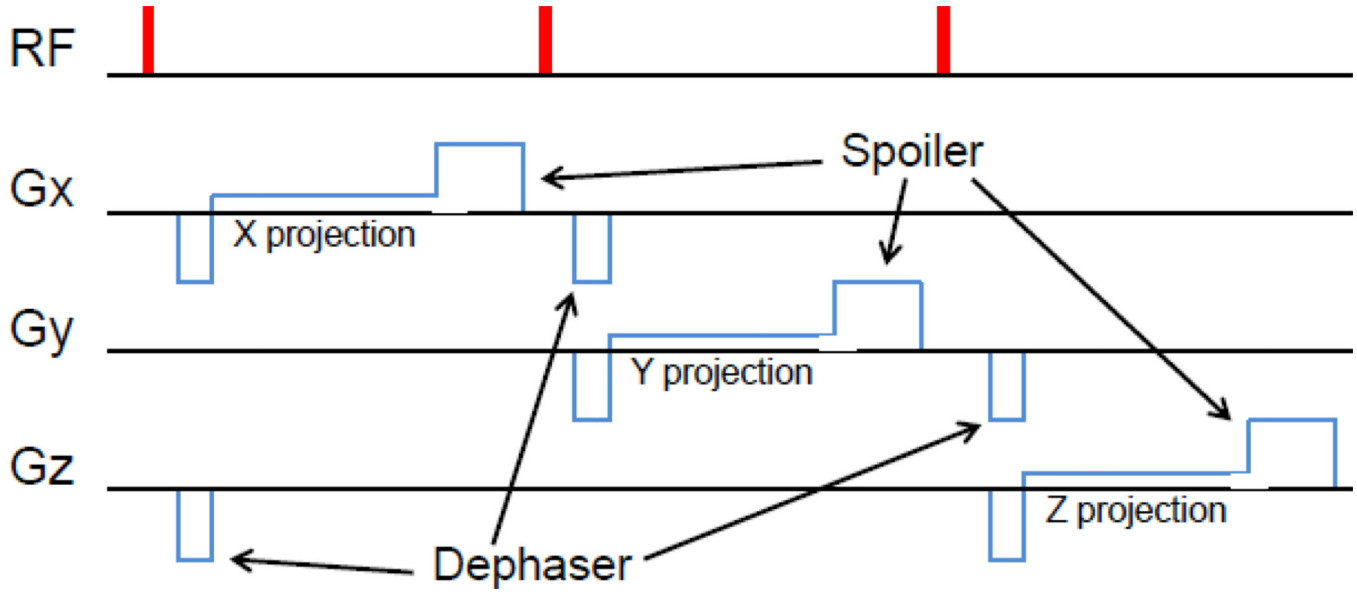

Figure 2. Tracking sequence module

The schematic plot of the wireless MR active marker tracking pulse sequence module.

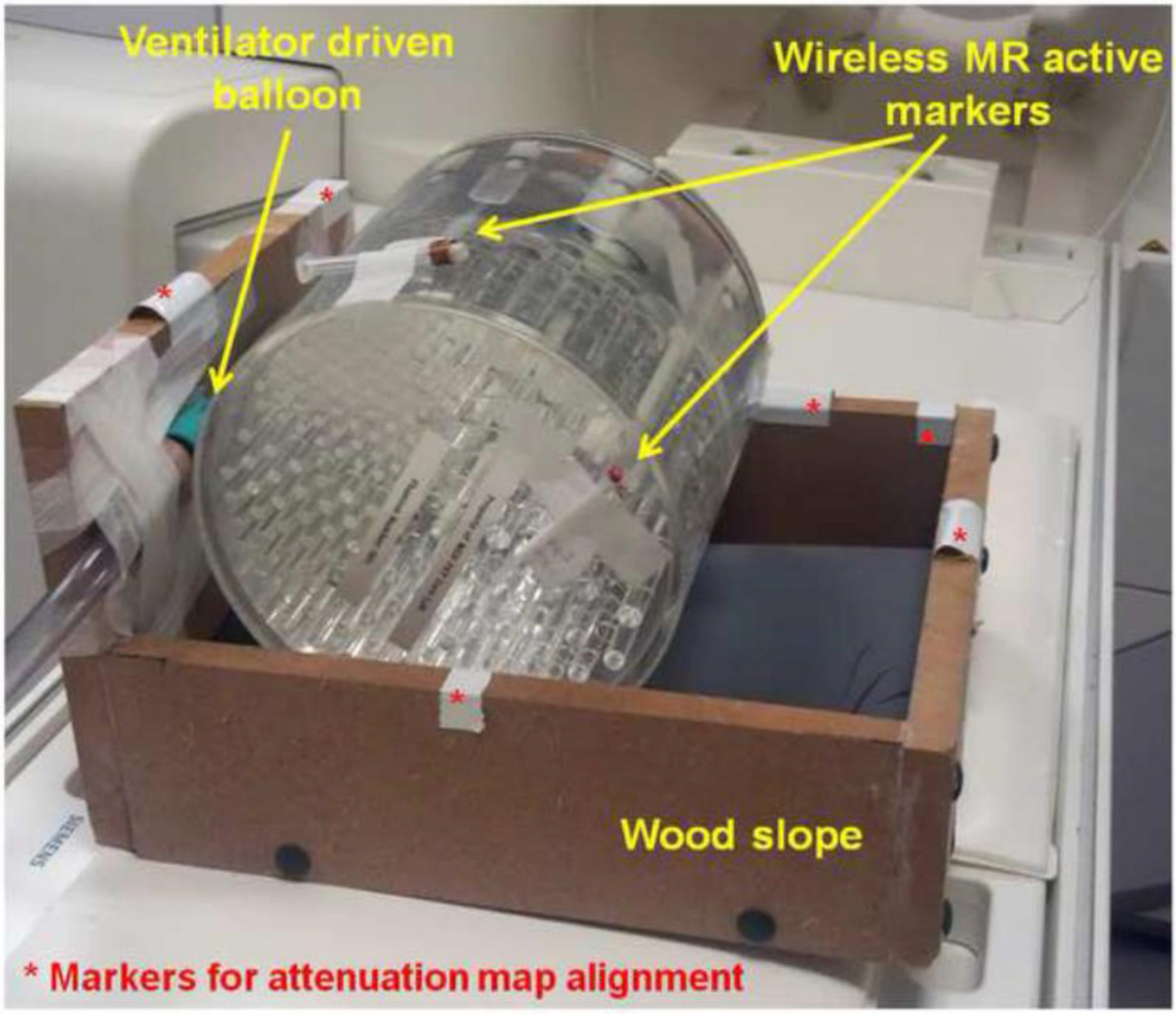

Figure 3. Setup of the phantom experiment

Three wireless MR active markers were placed on the surface of the ACR phantom (one the three markers was invisible in this photo).

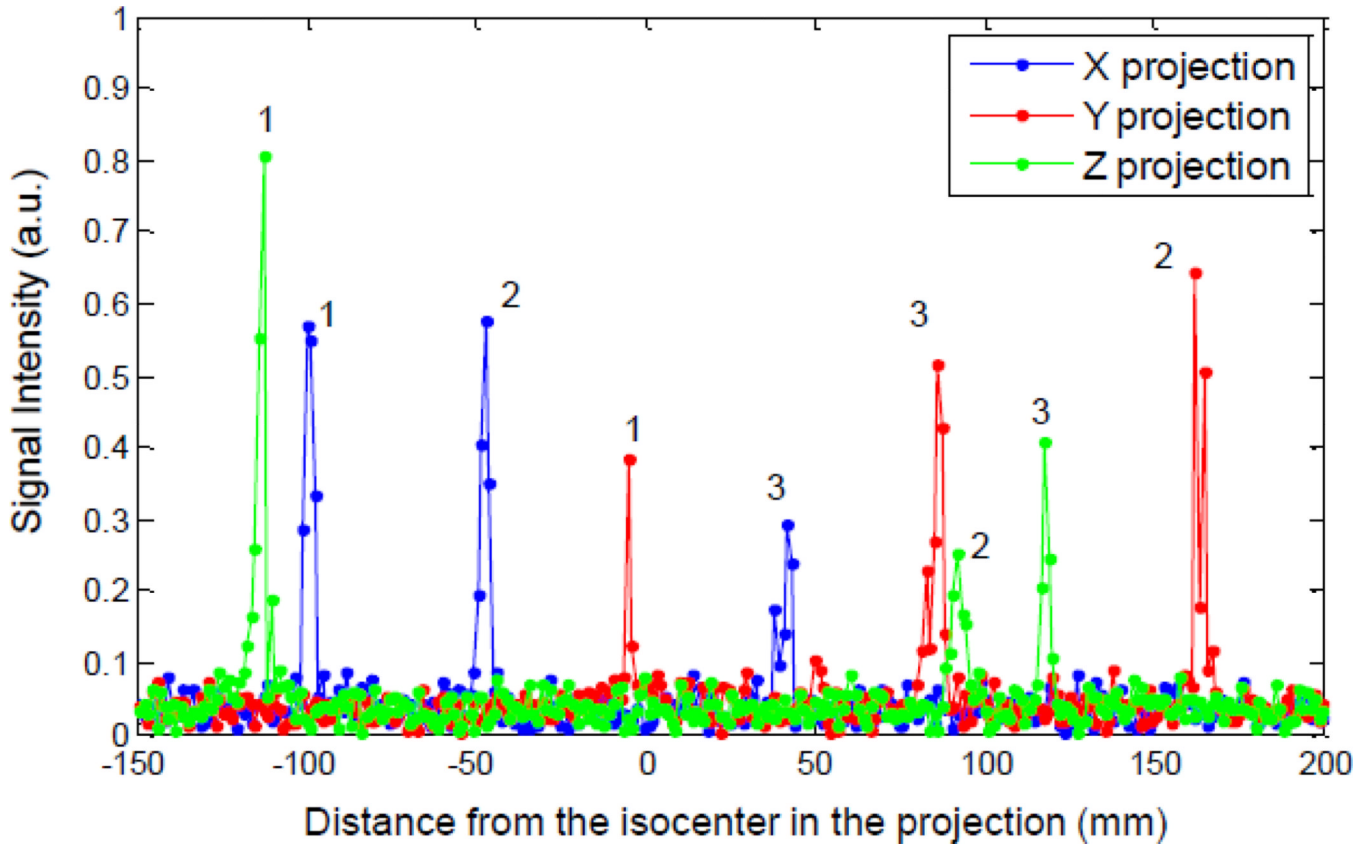

Figure 4. Marker projections

One set of X, Y, Z projection data of the active markers 1, 2 and 3 acquired using the tracking MR sequence module.

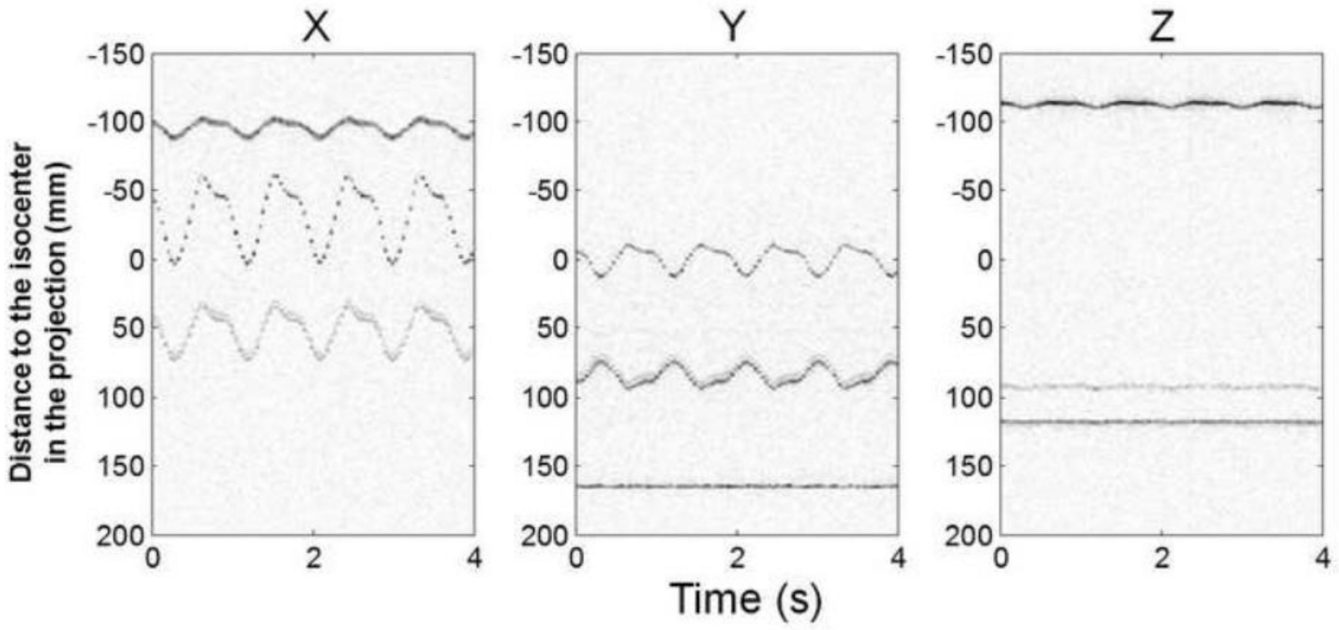

Figure 5. Marker traces

Traces of the three wireless active markers in the X, Y, Z projections in a 4 s period.

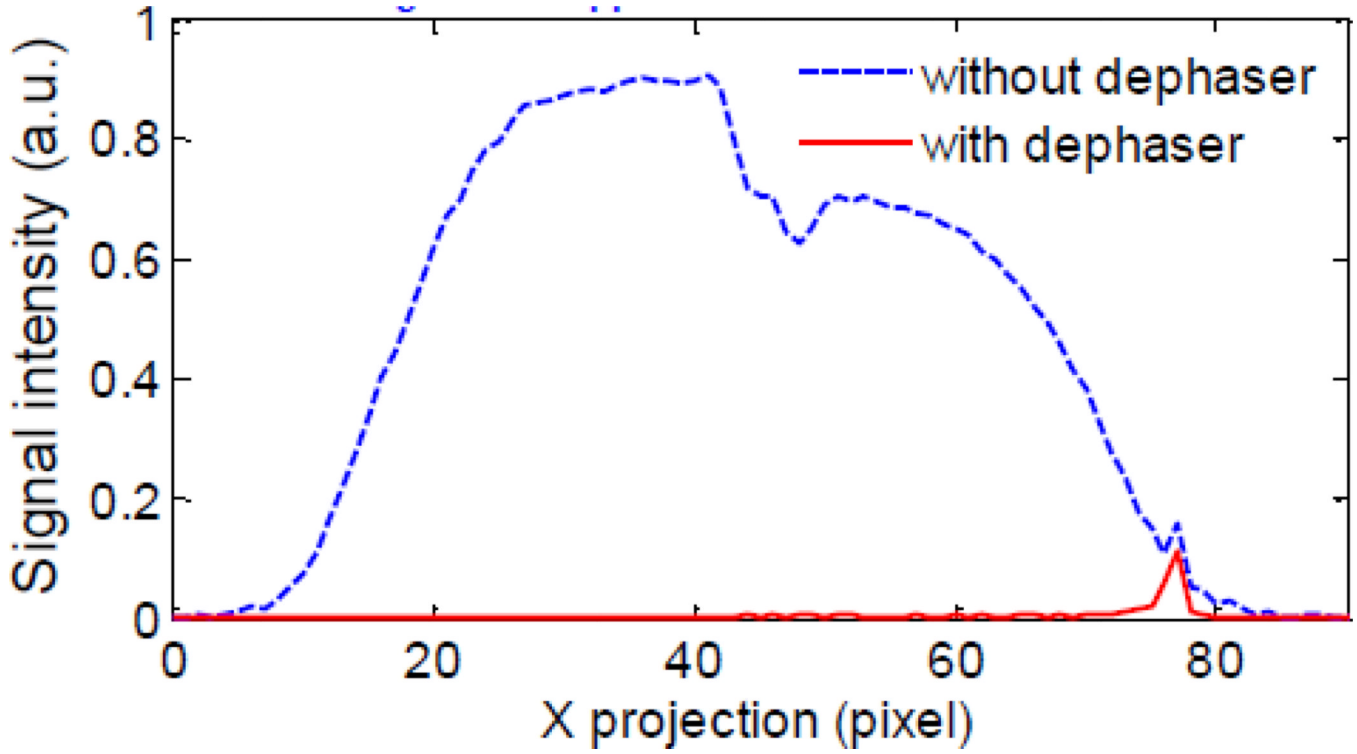

Figure 6. Effect of the dephaser gradients

The acquired projections of a wireless marker attached to a water phantom with and without dephaser.

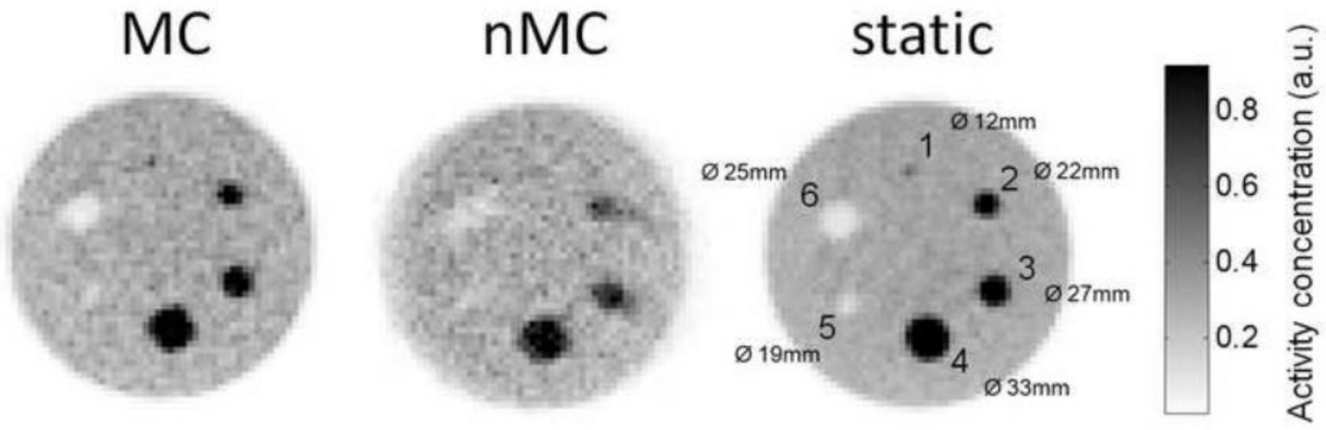

Figure 7. Reconstructed phantom images

The image of the phantom reconstructed from one noise realization with (MC) wireless marker based motion correction and without (nMC) motion correction. A static image (static) with 10 times more event counts is also shown as a reference. Note that the sphere diameter showing here are the outer diameters.

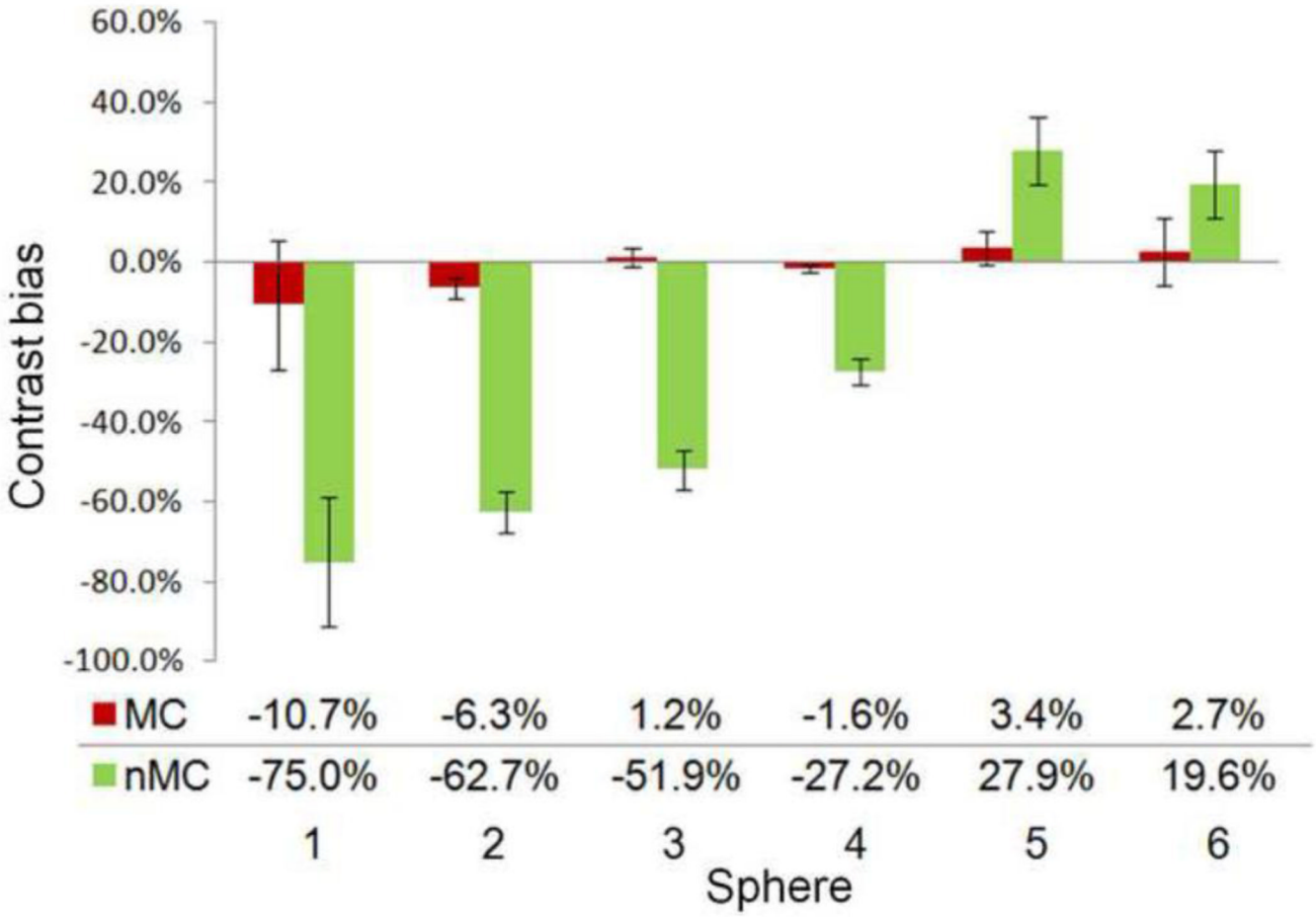

Figure 8. Contrast biases

The means and standard deviations of the contrast value biases of the 6 spheres in the reconstructed MC and nMC image volumes calculated from 24 noise realizations. The static reference image with approximately 10 times more event counts was used as the gold standard. The numbering of the spheres is shown in Figure 6.

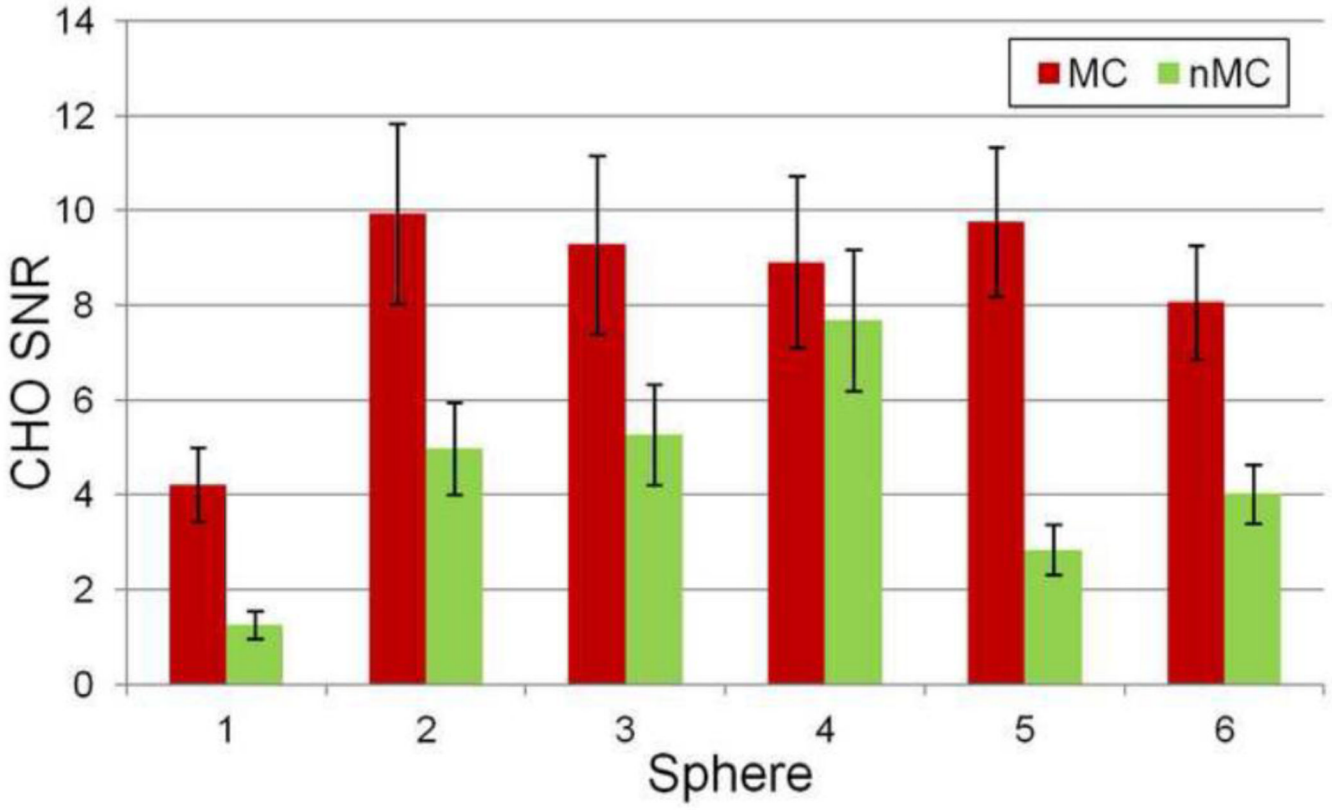

Figure 9. CHO SNR

The means and standard deviations of CHO SNR of the spheres using the images reconstructed with MC and nMC from the 24 noise realizations.

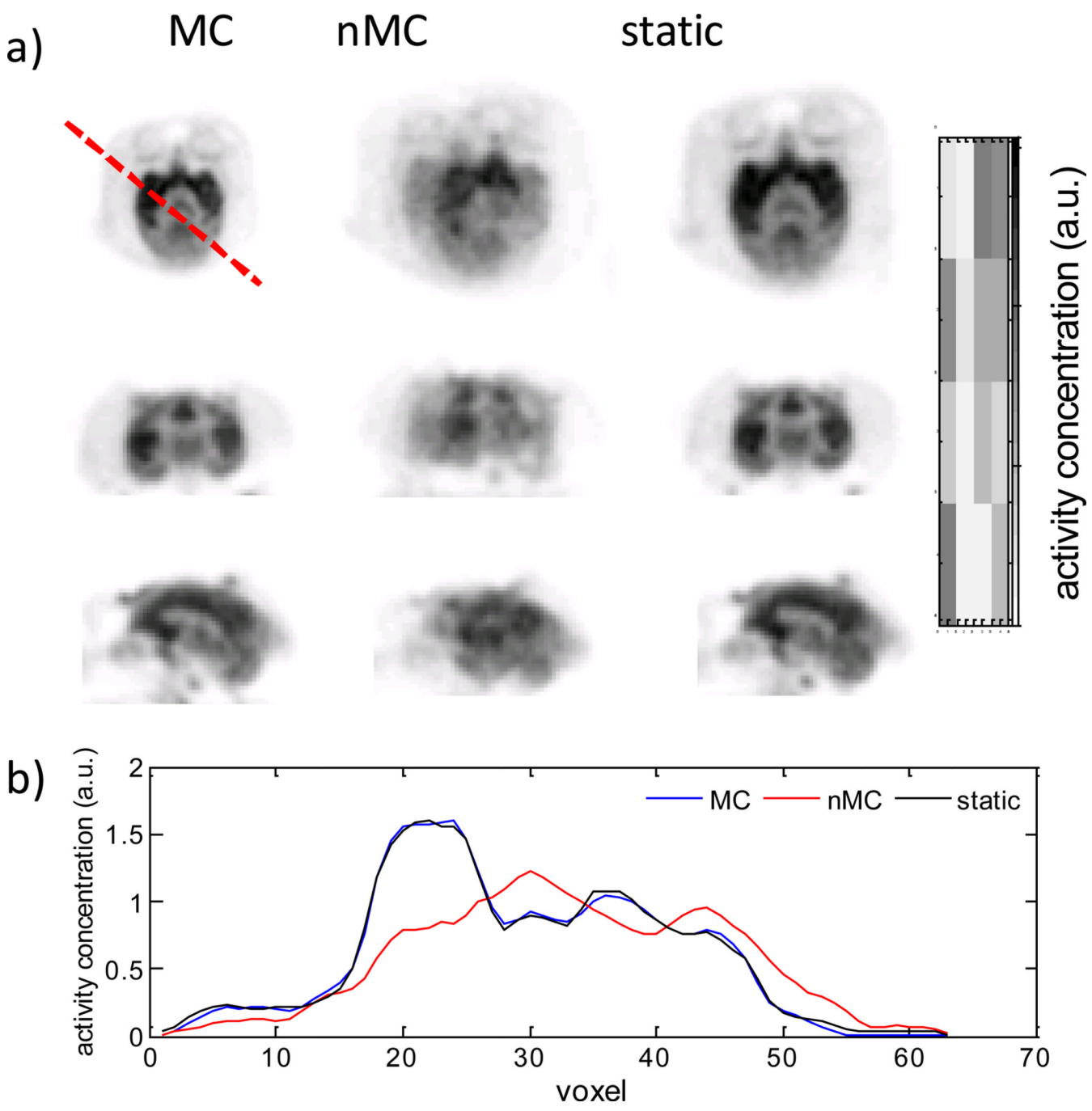

Figure 10. Reconstructed non-human primate images and line profiles

a) (top row) Axial, (middle row) coronal and (bottom row) sagittal slices of the image volume reconstructed using MC and nMC reconstruction from the same data set with introduced motion compared with the corresponding slices from the static reference image. b) Profiles along the dotted line in top left panel of a) from MC and nMC image volumes compared with the profile obtained from the static reference image volume.